SCIENCE CHINA
Information Sciences

• RESEARCH PAPER •

February 2026, Vol. 69, Iss. 2, 122401:1–122401:12
https://doi.org/10.1007/s11432-025-4629-0

T-type differential Helmholtz photoacoustic cell with microphone array for simultaneous multi-gas monitoring at ppb level

Zhuobei DENG[1†], Yafei LI[1*†], Yanxiong GUAN[1], Chen HUANG[1], Yanyu JIANG[2], Yifan WANG[2], Wanling DENG[1], Junkai HUANG[1], Chuantao ZHENG[3] & Tuan GUO[2*]

[1]*Department of Electronic Engineering, College of Information Science and Technology, Jinan University, Guangzhou 510630, China*
[2]*Institute of Photonics Technology, College of Physics and Optoelectronic, Engineering, Jinan University, Guangzhou 511443, China*
[3]*State Key Laboratory of Integrated Optoelectronics, College of Electronic Science and Engineering, Jilin University, Changchun 130012, China*

Received 27 July 2025/Revised 10 September 2025/Accepted 15 October 2025/Published online 9 January 2026

Abstract Multi-gas detection plays an important role in the fields of industrial safety and environmental protection. Currently, achieving simultaneous and high-precision detection of multiple gases faces many challenges. To solve this problem, a T-type differential Helmholtz photoacoustic (PA) cell integrated with an 8-microphone array was developed. The specially designed T-type differential Helmholtz structure enables signal enhancement and noise suppression. Furthermore, through the signal superposition and differential effects among the eight-microphone symmetrical array, the signal-to-noise ratio (SNR) is improved by ∼3.64 times compared with the single-microphone configuration, achieving high-sensitivity gas detection at the ppb level. The developed sensor was used to simultaneously measure two typical gases (CH_4 and C_2H_2). Experimental results show that the sensor has excellent linearity, high stability, and remarkable sensitivity, achieving a limit of detection (LoD) of 402 ppb for CH_4 with a normalized noise equivalent absorption (NNEA) coefficient of 4.18×10^{-9} $cm^{-1}\cdot W\cdot Hz^{-1/2}$, and a LoD of 254 ppb for C_2H_2 with a NNEA coefficient of 1.52×10^{-9} $cm^{-1}\cdot W\cdot Hz^{-1/2}$. Therefore, this novel and compact gas measurement device is expected to play an important role in fields such as industrial safety monitoring and environmental pollution control.

Keywords photoacoustic spectroscopy, gas detection, high-sensitivity, Helmholtz photoacoustic cell, microphone array

Citation Deng Z B, Li Y F, Guan Y X, et al. T-type differential Helmholtz photoacoustic cell with microphone array for simultaneous multi-gas monitoring at ppb level. Sci China Inf Sci, 2026, 69(2): 122401, https://doi.org/10.1007/s11432-025-4629-0

1 Introduction

Methane (CH_4) and acetylene (C_2H_2) are two common hydrocarbon gases with significant industrial applications but notable safety hazards and environmental risks. As the primary component of natural gas, CH_4 is widely used in energy production and chemical processing, yet its high flammability may cause explosions [1–4]. C_2H_2 is commonly used in metal welding and cutting, posing a threat to human health due to its instability and toxicity [5–8]. While minor fractions of both gases originate from natural processes (e.g., microbial activity in wetlands and plant metabolism), the majority of emissions stem from anthropogenic activities, including fossil fuel extraction, industrial leaks, and chemical production. In addition to the risks of fire and explosion, CH_4, as a potent greenhouse gas, also exacerbates the greenhouse effect, and C_2H_2 may cause acute poisoning through narcotic and asphyxiating effects [9–12]. Therefore, developing highly sensitive and selective gas sensors for simultaneous CH_4 and C_2H_2 detection is critical for industrial safety monitoring, environmental pollution control, and occupational health protection. Compared with the traditional electrochemical, catalytic combustion, and semiconductor gas detection technologies, infrared absorption spectroscopy gas detection technologies exhibit better selectivity, sensitivity and long-term stability [13–15]. Common infrared absorption spectroscopy gas detection technologies include direct absorption spectroscopy (DAS), tunable diode laser absorption spectroscopy (TDLAS) [16–18], off-axis integrated cavity output spectroscopy (OA-ICOS), and photoacoustic spectroscopy (PAS) [19–21]. It is always challenging to develop cost-effective methods for detecting multi-gases integrally in specific application environments. To overcome this arduous technical issue, quantum cascade laser based dual-spectroscopy technique [22], self-calibrated

* Corresponding author (email: liyafei@jnu.edu.cn, tuanguo@jnu.edu.cn)
† These authors contributed equally to this work.

$2f/1f$ wavelength modulation spectroscopy [23], quartz tuning fork (QTF) enhanced laser spectroscopy and multi-resonance photoacoustic spectroscopy [24,25], have been successfully demonstrated for three or more gases detection simultaneously. Among these technologies, PAS demonstrates distinct advantages due to its unique detection mechanism. By employing acoustic sensing, PAS avoids the optical path interference in traditional optical methods. It has a simple and robust structure that can achieve sensitivity at the parts per billion (ppb) level, making it ideal for long-term industrial monitoring [26–28]. The core principle of PAS gas detection technology is the photoacoustic (PA) effect. When gas molecules absorb modulated laser light, periodic pressure waves are generated in the PA cell, which are collected by high-sensitivity acoustic detectors. The innovative approach, which converts molecular absorption into acoustic detection, preserves spectroscopic specificity while addressing the vulnerability of optical components in harsh environments, establishing PAS as an emerging solution for trace gas detection.

The PA cell, serving as the core region for the interaction between excitation light and target gases, critically determines the PA signal generation efficiency through its structural design. Current mainstream resonant PA cell configurations encompass three canonical types: H-type, T-type, and Helmholtz-type [29–32]. Advancements have spurred the development of novel PA cells with enhanced signal acquisition capabilities. Wu et al. [33] proposed a novel fiber-optic PA sensor based on a 3D-printed non-destructive H-type resonator, which overcomes the necessity to compromise resonator integrity during signal measurement inherent in traditional H-type designs and achieves a CH_4 detection limit of 894 ppb. However, H-type PA cells are characterized by large volumes and susceptibility to environmental noise interference. In contrast, T-type PA cells offer more compact structures while exhibiting higher detection sensitivity at equivalent volumes. Feng et al. [34] developed a high-sensitivity and miniaturized T-type PA gas sensor, which effectively reduced flow noise and amplified the PA signals by optimizing the geometric refinement of the transition section between the buffer cavity and the resonator cavity, achieving a C_2H_2 detection limit of 278 ppb. Nevertheless, the single-buffer-cavity design of T-type PA cells struggles to fully isolate low-frequency vibrational disturbances, remaining vulnerable to environmental noise and consequently degrading the signal-to-noise ratio (SNR). Differentially configured Helmholtz PA cells can counteract environmental vibrations, flow perturbations, and other noise sources, thereby enhancing SNR. Ma et al. [35] fabricated a Helmholtz PA cell with a volume only 1/16 that of traditional H-type PA cells, and experimental results showed that the detection limit of hydrogen sulfide (H_2S) was 460 ppb. Wang et al. [36] designed a Helmholtz PA cell with a volume of 0.5 mL, which adopted a dual-connecting-pipe structure to suppress gas flow noise and achieve a C_2H_2 detection limit of 300 ppb. However, the Helmholtz PA cells suffer from non-uniform sound pressure distribution at resonant frequencies, resulting in a weakened PA signal and insufficient noise suppression capabilities. Therefore, structural optimization is crucial for concentrating sound pressure at specific focal points to improve the SNR of the sensor system.

In order to solve the problems existing in PA cells, this study integrates design concepts from both T-type and Helmholtz-type PA cells. A novel method is proposed to enhance the sensitivity of the sensor system by designing a T-type differential Helmholtz microphone array (TDHMA) PA cell integrated with eight microphones. The structure of the designed PA cell modifies a traditional Helmholtz PA cell by incorporating eight resonator cavities, and the cavities form eight distinct T-type elements integral to the cell. A micro-electro-mechanical system (MEMS) microphone is mounted at the end of each resonant cavity to detect the localized PA signal, which is processed by dedicated summing circuits. These circuits have the characteristics of small size, low power consumption, and high response speed, meeting the standards and portability requirements of real-time monitoring. The output signals of the four in-phase microphones were added, the output signals of the other four anti-phase microphones were added, and then the two anti-phase total output signals were differentiated. Compared with the traditional Helmholtz PA cells, the designed TDHMA PA cell can effectively concentrate the sound pressure at the ends of the eight resonator cavities, which can significantly enhance PA signals and suppress noise. The noise refers to the airflow noise that occurs simultaneously in the two buffer cavities due to uneven airflow or pressure fluctuations, and the common-mode environmental noise caused by the same interference to the two buffer cavities due to external environmental factors.

2 Design and optimization of PA cell

2.1 PA cell structure

Figure 1(a) depicts the structural schematic of the developed TDHMA PA cell. Eight resonant cavities were integrated onto the walls of two buffer cavities, and an MEMS microphone was mounted at the end of each resonator cavity to detect the PA signal. The special design shifts the position of the maximum sound pressure in the PA

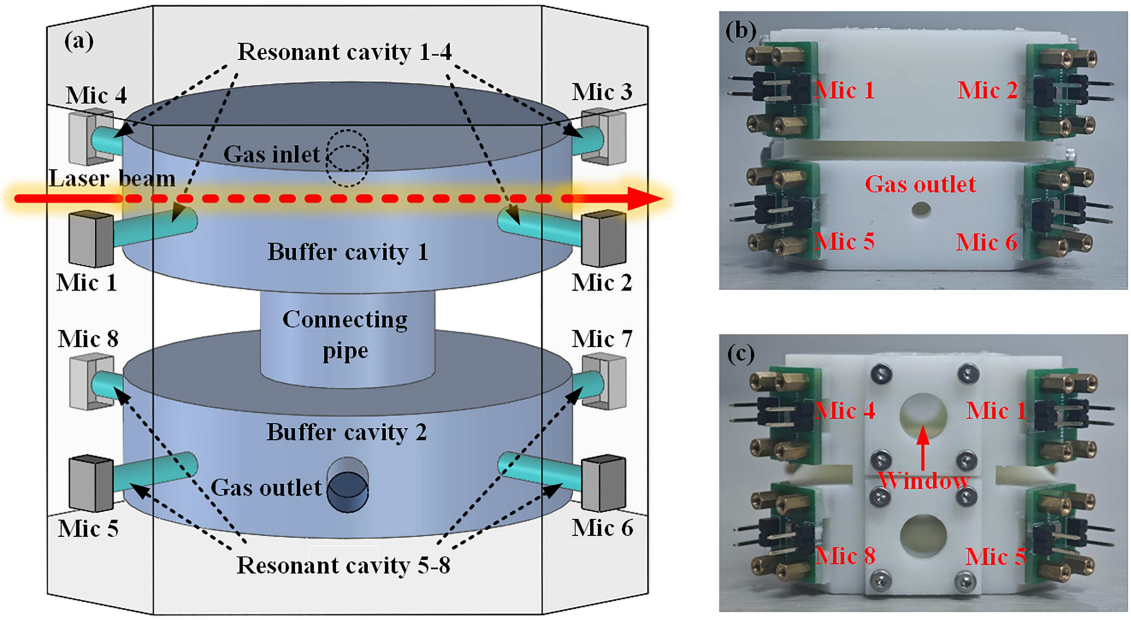

Figure 1 (Color online) (a) The structure diagram, (b) the front view and (c) the left view of the TDHMA PA cell.

cell to the ends of the resonator cavities, which is beneficial to the collection of sound pressure and significantly improves the amplitude of the sound pressure. Two optical windows were installed on the left- and right-side walls of the buffer cavity to facilitate the entry of the laser beam. In addition, a gas inlet was incorporated into the rear wall of buffer cavity 1 and a gas outlet was incorporated into the front wall of buffer cavity 2, ensuring efficient gas flow throughout the entire PA cell. Figures 1(b) and (c) display photographs of the TDHMA PA cell, which are the front view and the left side view, respectively. Compared to the traditional Helmholtz PA cell, the TDHMA PA cell can achieve a substantial improvement in the SNR of the sensor system without a significant increase in overall volume.

2.2 Detection theory

The PAS is a highly sensitive detection technology based on the PA effect, and its excellent detection sensitivity enables trace gas analysis to reach the level of ppb. The technology employs a modulated light source to illuminate the gas sample, and then the gas molecules absorb the light energy, resulting in periodic thermal expansion, which in turn generates sound waves [37–39]. The amplitude of the PA signal depends on parameters such as optical power, the sensitivity of the microphone and the cell constant of the PA cell [40,41], which can be expressed by (1), namely

$$S = S_0 P_{\text{eff}} C_{\text{cell}} c \alpha, \tag{1}$$

where S_0 is the sensitivity of the microphone, P_{eff} is the optical power, c is the gas concentration, α is the gas absorption coefficient, and C_{cell} is the cell constant of the PA cell, which quantifies the efficiency of the PA cell structure's response to acoustic pressure signals. The cell volume directly influences the acoustic energy accumulation and attenuation characteristics. The resonant frequency, determined by the cavity dimensions, is matched to the laser pulse frequency to optimize signal output and increase C_{cell}. The acoustic impedance of the cell wall material also affects acoustic wave transmission loss, thereby varying the C_{cell} value.

The schematic of the TDHMA PA cell and its supporting signal processing circuit are shown in Figure 2(a). The sound signals at microphones 1–4 are defined as x_1, x_2, x_3, and x_4, all of which have the same phase. The signals at microphones 5–8 are defined as x_5, x_6, x_7, and x_8, which are 180° out of phase with microphones 1–4. Figures 2(b) and (c) respectively show the schematic diagram and the physical diagram of the addition circuit. The method of taking differences first and then summing will use more addition circuits, which inevitably introduces more noise. Therefore, we adopt the method of summing first and then taking differences. The addition circuit is used to sum the signals from microphones 1–4 and microphones 5–8, respectively, and the output signals x_{output1} and x_{output2} can be expressed by (2) and (3), namely

$$x_{\text{output1}} = \frac{11}{5}(x_1 + x_2 + x_3 + x_4), \tag{2}$$

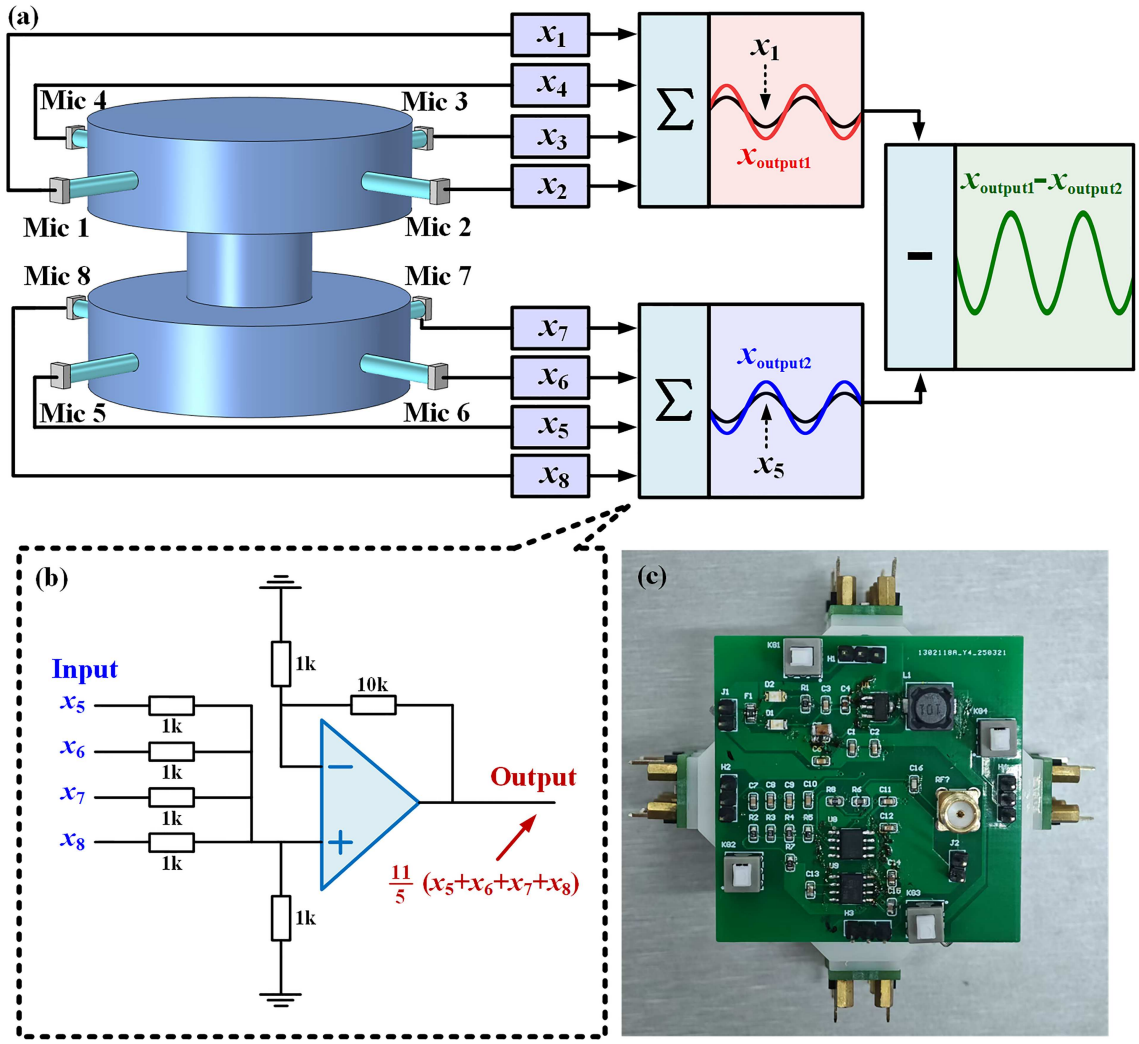

Figure 2 (Color online) (a) The schematic of the TDHMA PA cell and its supporting signal processing circuit. (b) The schematic diagram and (c) the physical diagram of the addition circuit. Mic: microphone.

$$x_{\text{output2}} = \frac{11}{5}(x_5 + x_6 + x_7 + x_8). \tag{3}$$

The signals x_{output1} and x_{output2} are then routed to input channels A and B of the lock-in amplifier, respectively. The obtained differential signal x_{output} can be described by (4), namely

$$x_{\text{output}} = x_{\text{output1}} - x_{\text{output2}} = \frac{11}{5}[(x_1 + x_2 + x_3 + x_4) - (x_5 + x_6 + x_7 + x_8)]. \tag{4}$$

Given the axisymmetric structure of the TDHMA PA cell, the sound signals captured by microphones 1–4 are identical, and those captured by microphones 5–8 are also identical. Therefore, Eqs. (2) and (3) can be simplified to (5) and (6), respectively, namely

$$x_{\text{output1}} = \frac{11}{5}nx_1, \tag{5}$$

$$x_{\text{output2}} = \frac{11}{5}nx_5, \tag{6}$$

where n represents the number of microphones within a single buffer cavity, which is set to 4. To compute the SNR of the sensor, the noise characteristics of the microphone array must be analyzed. When the signals from two in-phase microphones are added together, the total signal amplitude simply adds because the in-phase signals are correlated, meaning the PA signal increases by a factor of 2. Noise is a random signal that typically satisfies statistical independence. The total noise power is the sum of the two power values, and the effective value of noise is the square root of the power, so the noise increases by a factor of $\sqrt{2}$ [42]. Expanding the number of microphones

to n, the amplitude of the coherent signal becomes n times that of a single microphone, and the output white noise N_{output} can be calculated according to (7), namely

$$N_{\text{output}} = \frac{11}{5}\sqrt{n}N, \tag{7}$$

where N denotes the noise level of a single microphone. The signal-to-noise ratio of a single microphone output signal is defined as SNR_1, which can be represented by (8). Similarly, the signal-to-noise ratio of microphones 1–4 output signals is defined as SNR_{output1}, which can be represented by (9).

$$SNR_1 = \frac{x_1}{N}, \tag{8}$$

$$SNR_{\text{output1}} = \frac{x_{\text{output1}}}{N_{\text{output1}}} = \sqrt{n}\frac{x_1}{N}, \tag{9}$$

where N_{output1} represents the noise level of microphones 1–4 output signal x_{output1}. As derived from (9), compared to a single microphone, there is a 2-fold improvement in the output signal-to-noise ratio when a 4-microphone array is used. When considering the differential output of the PA cell with an 8-microphone array, the SNR_{output} is expressed by (10), namely

$$SNR_{\text{output}} = \frac{x_{\text{output}}}{N_{\text{output1}} - N_{\text{output2}}}, \tag{10}$$

where N_{output2} represents the noise level of microphones 5–8 output signal x_{output2}. In the differential output mode of the PA cell, the PA signals are anti-phase while the noise components are in-phase. Therefore, the values of N_{output1} and N_{output2} are theoretically equal, and SNR_{output} is infinite. In practical applications, due to the noise introduced by the addition circuit and the inherent background noise of the microphone are different, N_{output1} and N_{output2} are not equal but the difference in values is not large. Therefore, in the differential output mode, the SNR of the output signal is significantly improved, thereby substantially improving the detection sensitivity of the sensor system.

2.3 Simulation analysis and parameter optimization

The traditional Helmholtz PA cell consists of an upper and a lower cylindrical cavity connected by a connecting pipe [43]. At the resonant frequency, the position of the maximum sound signal is located on the side walls of the upper and lower cylindrical cavities, which is the optimal location for installing the microphone. However, the minimal sound pressure variation across different positions within traditional Helmholtz PA cell results in relatively weak pressure signals detected by microphones. To address this limitation, four resonant cavities were added to each cylindrical cavity in this study, forming a T-type structure that concentrates sound pressure at the end of the resonance cavities. Figures 3(a) and (b) show the PA field distribution cloud maps of the traditional Helmholtz PA cell and the TDHMA PA cell simulated using COMSOL software, respectively. The PA cell structure was modeled using the ultra-fine free tetrahedral mesh, and its frequency domain characteristics were simulated by the pressure acoustics module. The boundary conditions were set as hard sound field walls, and a line source simulated the incident laser beam governed by (11), namely

$$\nabla \cdot \left(-\frac{1}{\rho_{\text{c}}}\nabla p\right) - \frac{\omega_0^2}{\rho_{\text{c}} v^2} p = I_{\text{Q}}\delta\left(r_1 - r_2\right), \tag{11}$$

where ρ_{c} is the fluid density; p is the complex sound pressure; ω_0 is the angular frequency; v is the speed of sound; I_{Q} is the source intensity of the line source, which is set to 1 $\text{m}^2 \cdot \text{s}^{-1}$; $\delta\left(r_1 - r_2\right)$ is the Dirac delta function, where r_1 represents the observation position and r_2 denotes the source position. The TDHMA PA cell consists of eight resonant cavities, two buffer cavities, and one connecting pipe. The connecting pipe connects the two buffer cavities, and four resonant cavities are mounted on the side walls of each buffer cavity, thus forming a combined T-type differential Helmholtz structure. Simulation results show that this configuration transfers the maximum sound pressure to the distal ends of the resonant cavities, namely the positions marked as B1 and B2 in Figure 3(b).

Optimizing the parameters of the TDHMA PA cell can enhance the amplitude of the PA signal. The dimensions of the buffer cavities and resonant cavities exert a prevailing influence on the sound pressure in the PA cell, while the influence of the connecting pipe on the sound pressure can be ignored. In order to miniaturize the PA cell, the length and radius of the connecting pipe were set to 10 and 7 mm, respectively. Figure 3(c) shows the structural

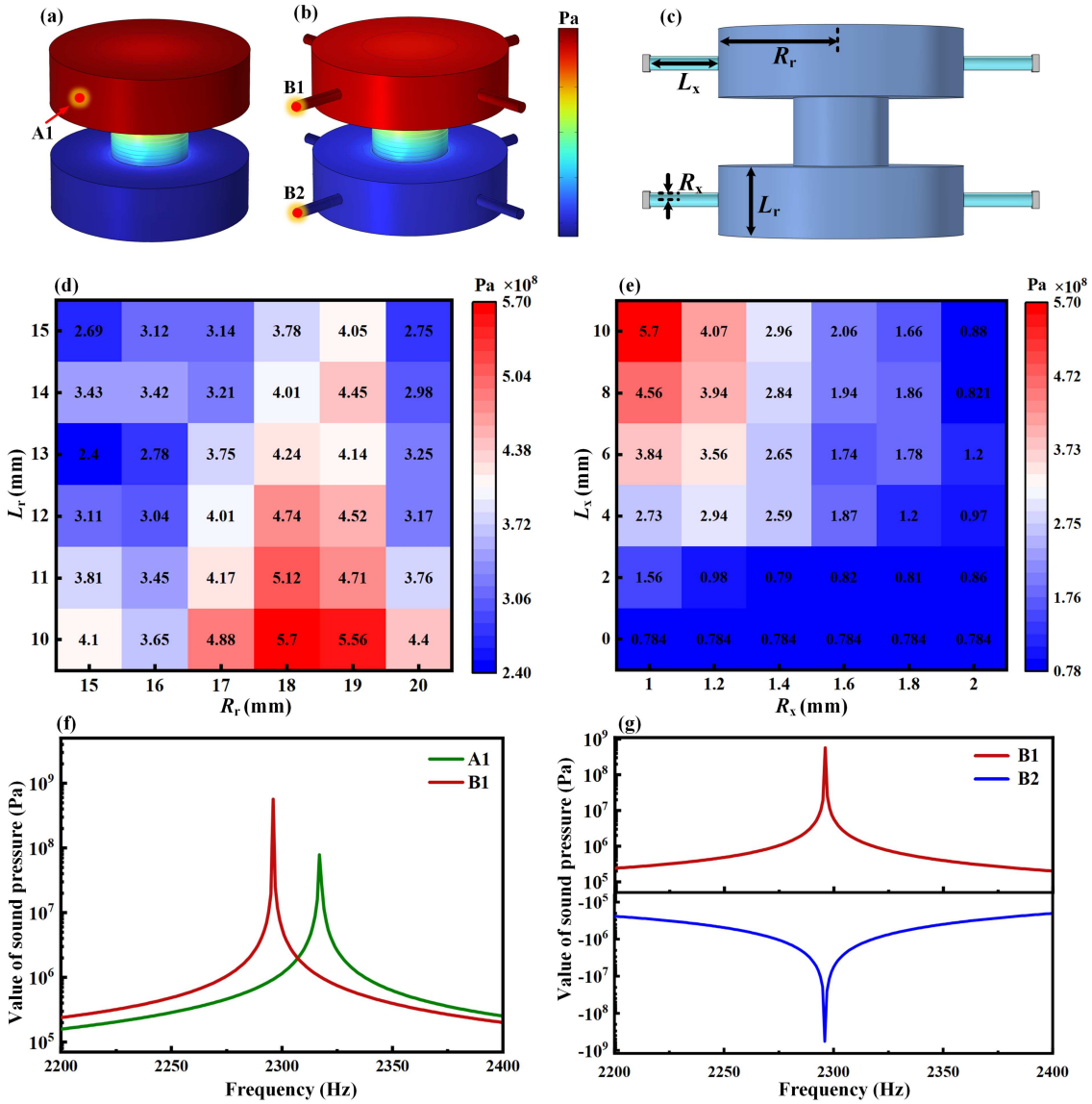

Figure 3 (Color online) PA field distribution cloud maps of (a) the traditional Helmholtz PA cell and (b) the TDHMA PA cell. (c) Structural schematic diagram of the TDHMA PA cell. (d) The simulated sound pressure distribution of buffer cavity with different length L_r and radius R_r. (e) The simulated sound pressure distribution of resonant cavity with different length L_x and radius R_x. (f) The simulated frequency response curves of A1 and B1 in the range of 2200–2400 Hz. (g) The simulated frequency response curves of B1 and B2 of the TDHMA PA cell in the range of 2200–2400 Hz.

schematic diagram of the TDHMA PA cell, where R_r and L_r respectively represent the radius and length of the buffer cavities, and R_x and L_x respectively represent the radius and length of the resonant cavities. First, the radius R_r and the length L_r of the buffer cavities are optimized based on COMSOL software, with the simulation results shown in Figure 3(d). As R_r increases, the sound pressure P first rises and then declines. When R_r is 18 mm, P is maximum. In addition, P increases as L_r decreases. In the TDHMA PA cell, the quality factor Q is proportional to the volume of the two buffer cavities, and the volume of the buffer cavities must be significantly larger than the volume of the connecting pipe. Therefore, L_r cannot be too small and can be set to 10 mm. Then, the radius R_x and length L_x of the resonant cavities are optimized, and the simulation results are shown in Figure 3(e). P increases as R_x decreases, but due to physical size limitations, too small R_x prevents the microphone from receiving PA signals. If R_x is less than 1 mm, the opening at the end of the resonant cavity cannot completely cover the sensitive area of the microphone, which may result in incomplete sound pressure collection and a decrease in P. P increases as L_x increases, but too large L_x is not conducive to the miniaturization of the sensor. Taking all factors into consideration, L_x and R_x are set to 10 and 1 mm, respectively.

Frequency-domain simulations were conducted for both the traditional Helmholtz PA cell and the TDHMA PA

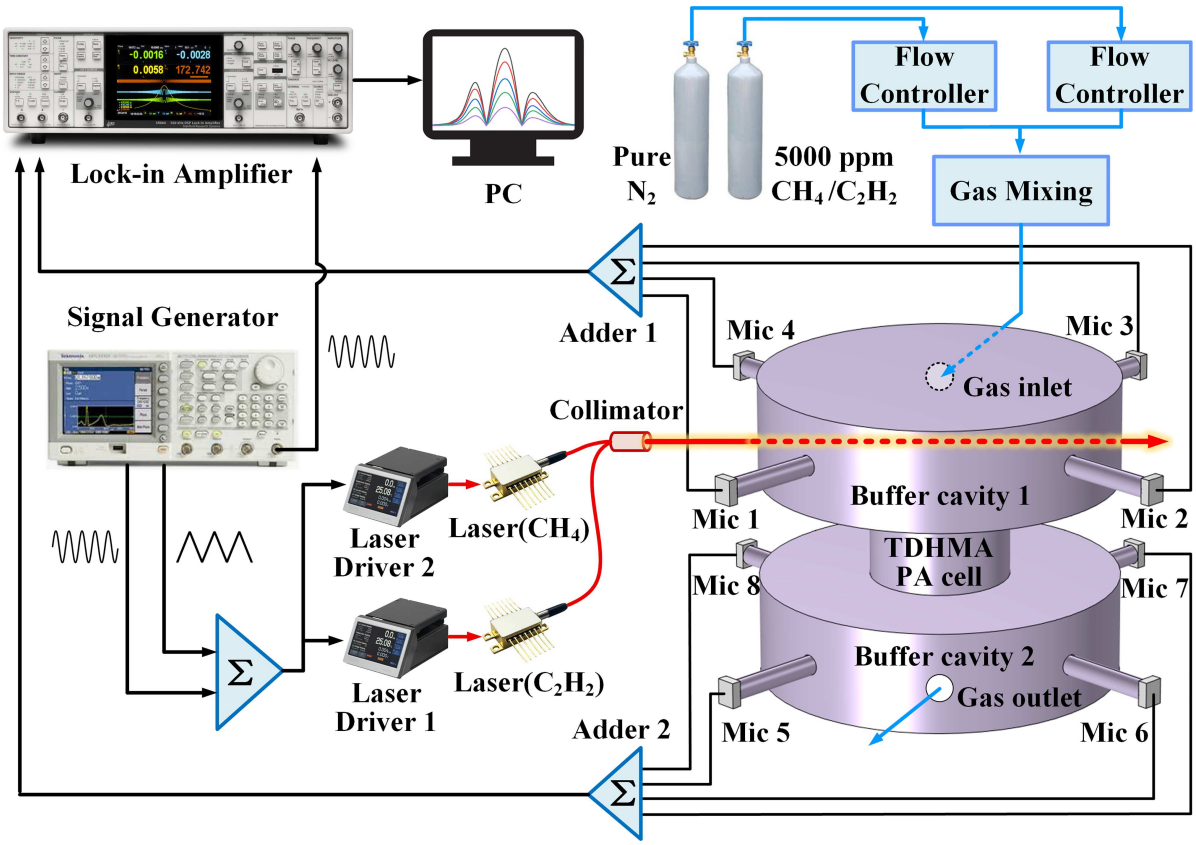

Figure 4 (Color online) Schematic diagram of the sensor system.

cell. Position A1 in Figure 3(a) indicates the location of maximum sound pressure at the resonant frequency for the traditional Helmholtz PA cell. Positions B1 and B2 in Figure 3(b) indicate the locations of maximum sound pressure at the resonant frequency for the TDHMA PA cell. The frequency response curves at A1 and B1 within the 2200–2400 Hz range are shown in Figure 3(f). The resonant frequencies of the traditional Helmholtz PA cell and the TDHMA PA cell are 2317 and 2296 Hz, respectively. Simulation results show that the signal of the TDHMA PA cell is enhanced by a factor of ∼7 compared with that of the traditional Helmholtz PA cell. The frequency response curves at B1 and B2 are shown in Figure 3(g), and it can be seen that the sound pressure at B1 and B2 has the same amplitude and opposite phase.

3 Sensing system and setup

Figure 4 depicts the schematic diagram of the sensor system. A laser driver (Thorlabs, model CLD1015, USA) with integrated current drive and temperature control supplied the driving current and stabilized the laser temperature at 25°. Two distributed feedback (DFB) lasers with central wavelengths of 1653.73 and 1532.68 nm were respectively used for CH_4 and C_2H_2 detection [44, 45]. A signal generator (GW Instek, model MFG-2260M, China) was used to provide the modulation signal and the reference signal. The modulation signal drove the DFB laser via the current driver, and the generated laser beam entered the buffer cavity 1 of the TDHMA PA cell perpendicularly through a window. The reference signal was directly sent to a lock-in amplifier (Stanford Research Systems, model SR860m, USA). Eight MEMS microphones (TDK, model ICS-40730, Japan) were installed at the ends of the eight resonant cavities to detect the PA signals generated by the periodic expansion and contraction of gas molecules after absorbing laser energy. The received PA signals were fed into the lock-in amplifier, where the $2f$ signals related to gas concentrations were extracted. The $2f$ signals were then transmitted to a personal computer (PC, DELL, model Dell G3, USA). Real-time dynamic monitoring of gas concentrations was performed using the monitoring platform based on LabVIEW software. A gas mixing system (Sevenstar, model CS300, China) prepared target gases CH_4 and C_2H_2 at various concentrations by blending 5000 ppm CH_4 and 5000 ppm C_2H_2 with pure nitrogen (N_2) in specific ratios. The gas inlet and gas outlet of the PA cell were respectively positioned on the rear wall of buffer

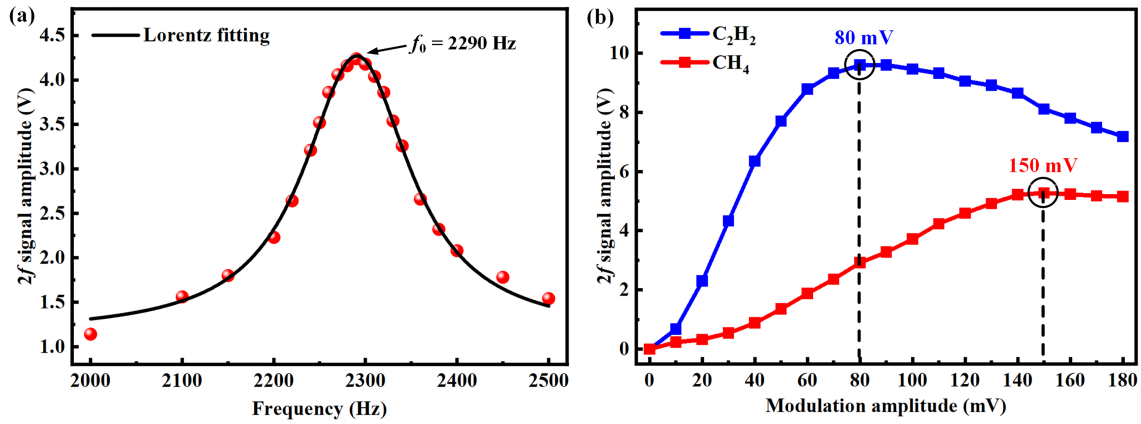

Figure 5 (Color online) (a) The frequency response curve of the TDHMA PA cell in the range of 2000–2500 Hz. (b) The $2f$ signal amplitudes measured under different modulation amplitudes for 5000 ppm CH_4 (red line) and 5000 ppm C_2H_2 (blue line).

cavity 1 and the front wall of buffer cavity 2, facilitating rapid gas flow through the PA cell to minimize response time.

4 Experimental results and analysis

4.1 Parameter optimization

The frequency response of the PA cell is affected by factors such as temperature, pressure, and machining precision, necessitating calibration prior to use [46]. Since the resonant frequency of the PA cell depends solely on its mechanical structure and is independent of the target gas species, 5000 ppm CH_4 was used to measure the $2f$ signal amplitude across modulation frequencies. As shown in Figure 5(a), the frequency response curve was fitted with a Lorentzian function in the range of 2000–2500 Hz. The maximum $2f$ signal amplitude occurred at 2290 Hz, corresponding to a laser modulation signal frequency of 1145 Hz. The measured resonant frequency is 2290 Hz and the simulated resonant frequency is 2296 Hz, showing a minor deviation of 0.26%. This deviation is primarily due to errors in the cavity length during machining. The elastic modulus of the cavity wall material used in the simulation is a theoretical value, and the window changes the curved structure of the cylindrical side. This deviation is within an acceptable range, and does not affect the performance of the PA cell. The $2f$ signal amplitude is also influenced by the sinusoidal modulation signal. The $2f$ signal amplitudes under different modulation amplitudes are shown in Figure 5(b). The red and blue curves represent the modulation amplitude optimization for CH_4 and C_2H_2, respectively, both exhibiting an initial increase followed by a decrease. The $2f$ signal amplitude peaked at the modulation amplitude of 150 mV for the CH_4 laser and 80 mV for the C_2H_2 laser.

4.2 Sensing performance and characteristics

To demonstrate the optimal performance of the TDHMA PA cell, the eight MEMS microphones were simultaneously activated for PA signal detection. Accurate quantification of target gas concentrations requires sensor calibration [47]. CH_4 and C_2H_2 gases of different concentrations were prepared using the gas mixing system and then sequentially introduced into the PA cell. The time-division multiplexing technology was adopted to detect CH_4 and C_2H_2 gases, respectively. Figure 6(a) shows the $2f$ signal waveforms at different CH_4 concentrations, and it can be seen that the amplitudes of the PA signals increase with the increase in CH_4 concentrations. The $2f$ signal amplitudes for different CH_4 concentrations are shown in Figure 6(b). As shown in Figure 6(c), the average values $A(CH_4)$ of $2f$ signal amplitudes at different CH_4 concentrations $C(CH_4)$ were calculated and linearly fitted, and the fitted line can be expressed by (12), i.e.,

$$A(CH_4) = 1.16 \times 10^{-1} + 1.07 \times 10^{-3} C(CH_4), \tag{12}$$

where the goodness of fit is 0.998. Figures 6(d) and (e) show the $2f$ signal and the noise signal away from the absorption peak for 2000 ppm CH_4, respectively. The amplitude of the $2f$ signal is 5.35 V and the standard deviation (1σ) of the noise signal is 0.43 mV. At this time, the SNR can be calculated as 12441 and the limit of detection (LoD) is determined to be 402 ppb. Figure 6(f) shows the $2f$ signal waveforms at different C_2H_2 concentrations,

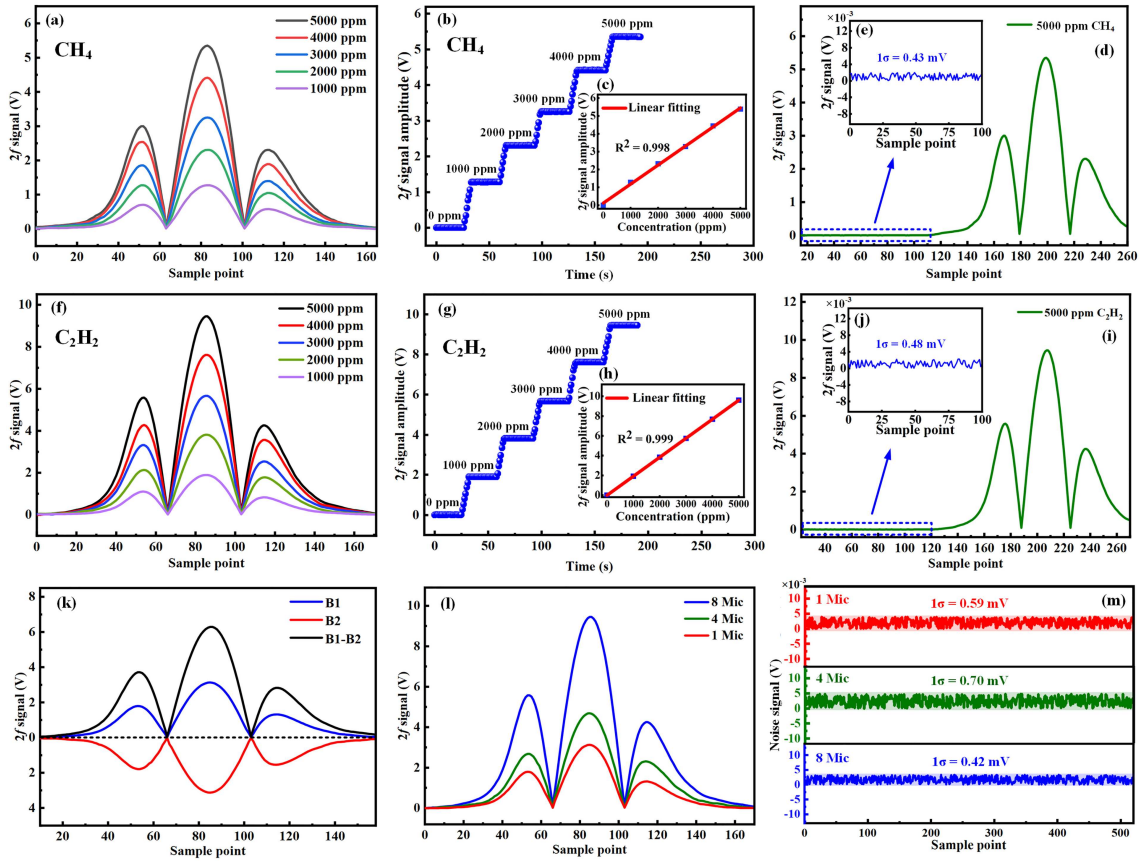

Figure 6 (Color online) (a) The waveforms and (b) the amplitudes of the $2f$ signal at different CH_4 concentrations. (c) The fitting line between CH_4 gas concentrations and the corresponding $2f$ signal amplitudes. (d) The $2f$ signal waveform and (e) the noise signal away from the absorption peak for 5000 ppm CH_4. (f) The waveforms and (g) the amplitudes of the $2f$ signal at different C_2H_2 concentrations. (h) The fitting line between C_2H_2 gas concentrations and the corresponding $2f$ signal amplitudes. (i) The $2f$ signal waveform and (j) the noise signal away from the absorption peak for 5000 ppm C_2H_2. (k) the $2f$ signal waveforms of 5000 ppm C_2H_2 in different mode configurations. (l) The $2f$ signal waveforms of 5000 ppm C_2H_2 under different numbers of microphones. (m) The background noise signals of 0 ppm C_2H_2 collected by using a single microphone, a 4-microphone array, and an 8-microphone array.

and the corresponding $2f$ signal amplitudes are shown in Figure 6(g). As shown in Figure 6(h), a linear fitting line was obtained between the average values $A(C_2H_2)$ of $2f$ signal amplitudes and the C_2H_2 concentrations $C(C_2H_2)$, i.e.,

$$A(C_2H_2) = 7.62 \times 10^{-3} + 1.92 \times 10^{-3} C(C_2H_2), \tag{13}$$

where the goodness of fit is 0.999. Figures 6(i) and (j) show the $2f$ signal and the noise signal away from the absorption peak for 5000 ppm C_2H_2, respectively. The amplitude of the $2f$ signal is 9.45 V and the 1σ value of the noise signal is 0.48 mV. Therefore, the SNR is 19687 and the LoD is determined as 254 ppb.

Normalized noise equivalent absorption (NNEA) coefficient is one of the important indicators for evaluating the performance of the PA gas sensor, which can be expressed by (14), i.e.,

$$\text{NNEA} = \frac{W \times A \times \text{LoD}}{\sqrt{2 \times \text{ENBW}}}, \tag{14}$$

where W is the output power of the laser, approximately 17 mW; ENBW is the detection bandwidth, which is related to the time constant and filter slope; A is the absorption coefficient, which can be obtained from the HITRAN database. For CH_4 absorption line at 1653.73 nm, the absorption coefficient is 0.306 cm^{-1}, while for C_2H_2 absorption line at 1532.68 nm, the absorption coefficient is 0.556 cm^{-1}. Therefore, the NNEA coefficients of CH_4 and C_2H_2 can be calculated to be 4.18×10^{-9} and 1.52×10^{-9} $cm^{-1}\cdot W\cdot Hz^{-1/2}$, respectively.

Figure 6(k) shows the $2f$ signal waveforms of 5000 ppm C_2H_2 in different mode configurations. The $2f$ signals at B1 and B2 in Figure 3(b) are collected, and it can be seen that the $2f$ signals P_{B1} and P_{B2} at B1 and B2 are equal in amplitude but opposite in phase. When P_{B1} and P_{B2} are differentially input into the lock-in amplifier, the obtained differential signal $P_{B1\text{-}B2}$ shows ~2 times enhancement. The $2f$ signals of the PA cell with different

Table 1 Performance comparison of sensors with different types of PA cells.

Cell type	Gas type	Optical power (mW)	Absorption line (nm)	LoD (ppb)	NNEA coefficient ($cm^{-1}\cdot W\cdot Hz^{-1/2}$)	Ref.
T-type	CH_4	30	1650.00	503	1.69×10^{-7}	[48]
	C_2H_2	20	1530.00	64	4.21×10^{-8}	
TT-type	CH_4	30	1650.96	250	1.1×10^{-8}	[49]
	C_2H_2	30	1531.58	77	8.4×10^{-9}	
Helmholtz	CH_4	2.5	7842.89	1050	2.01×10^{-8}	[50]
	C_2H_2	1000	1532.80	15	2.70×10^{-9}	[51]
TDHMA	CH_4	17	1653.73	402	4.18×10^{-9}	This paper
	C_2H_2	17	1532.68	256	1.52×10^{-9}	

numbers of microphone array were tested. When the number of microphones was increased from 1 to 4, the amplitude of the $2f$ signal theoretically increased by a factor of 1.6. For the TDHMA PA cell, the signals output from the 4-microphone array symmetrically above and below have the same amplitude and opposite phases, so the amplitude of the differential signal output from the 8-microphone array should be twice that of the signal output from the 4-microphone array. As shown in Figure 6(l), the amplitudes of the $2f$ signals of the actual acquired single microphone, 4-microphone array and 8-microphone array are 3.13, 4.74, and 9.45 V, respectively, which are basically the same as the theoretical value. To evaluate the noise suppression capability of the PA cell, 0 ppm C_2H_2 (pure N_2) was flowed through the PA cell at 100 sccm. As shown in Figure 6(m), the background noise signals were recorded under single microphone, 4-microphone array, and 8-microphone array configurations, and the 1σ values of the noise signals were 0.59, 0.70, and 0.42 mV, corresponding to SNRs of 5305, 6771, and 19286, respectively. The results indicate that the microphone array in the TDHMA PA cell enhances SNR, and the differential structure further improves noise suppression.

5 Discussion

Table 1 shows the performance comparison of the developed TDHMA PA cell with other reported PA cells. The key parameters, including LoD, NNEA coefficient, optical power and absorption line, provide a comprehensive basis for evaluating sensor performance. For CH_4 detection, the TDHMA PA cell achieves a LoD of 402 ppb, which outperforms the T-type PA cell but is slightly higher than the TT-type PA cell. However, the TDHMA PA cell exhibits a significantly lower NNEA coefficient compared to both T-type and TT-type cells. This indicates that the design of the TDHMA PA cell more efficiently converts optical power into detectable sound signals while minimizing noise. Notably, the TT-type cell relies on 30 mW optical power, whereas the TDHMA cell operates at 17 mW, demonstrating superior sensitivity under lower power consumption. In the case of C_2H_2 detection, the TDHMA PA cell achieves a LoD of 256 ppb with an NNEA coefficient of 1.52×10^{-9} $cm^{-1}\cdot W\cdot Hz^{-1/2}$. Although the LoD of the TDHMA cell is higher than that of the T-type, TT-type, and Helmholtz-type cells, when normalized by optical power, the NNEA coefficient is the lowest among all compared PA cells, highlighting its beneficial effects in signal amplification and noise suppression. The synergistic effect of the 8-microphone array and the differential Helmholtz structure contributed to amplifying coherent signals and suppressing common-mode noise.

6 Conclusion

In this study, a high-sensitivity gas sensor was developed based on the TDHMA PA cell for CH_4 and C_2H_2 detection. Building upon a traditional Helmholtz PA cell, eight T-type resonators were integrated into the sidewalls of two buffer cavities and an 8-microphone array was used to detect the PA signal. Through theoretical analysis of the microphone array and its peripheral circuitry, combined with finite element simulations, the geometric parameters of the TDHMA PA cell were optimized to maximize detection performance. Simulation results confirmed that the integration of T-type resonators with the Helmholtz structure significantly enhances PA signals by concentrating sound pressure at the ends of the resonators. The microphone array amplifies the coherent signals, and the differential structure suppresses the common mode noise, collectively achieving a substantial improvement in the SNR of the sensor system. The experimental results show that the 8-microphone array increases the PA signal by ∼3.02 times and improves the SNR by ∼3.64 times compared to the single-microphone configuration. Linear relationships between PA signals and gas concentrations were fitted. For CH_4, a LoD of 402 ppb and a NNEA coefficient of 4.18×10^{-9} $cm^{-1}\cdot W\cdot Hz^{-1/2}$ were achieved. For C_2H_2, the LoD and the NNEA coefficient were

256 ppb and 1.52×10^{-9} $cm^{-1}\cdot W\cdot Hz^{-1/2}$, respectively. In future work, the performance of the sensor system can be further improved by increasing the optical power, the number of microphones and the number of reflections.

Acknowledgements This work was supported by National Natural Science Foundation of China (Grant No. 62035006), National Key Research and Development Program of China (Grant No. 2024YFE0209200), Program of Marine Economy Development Special Fund (six marine industries) under Department of Natural Resources of Guangdong Province (Grant No. GDNRC [2024]16), Guangdong Basic and Applied Basic Research Foundation (Grant No. 2025A1515010112), Guangzhou Science and Technology Project (Grant No. 2025A04J2279), and Fundamental Research Funds for the Central Universities (Grant No. 21624346).

References

1 Zhu Y, Wu G, Guan Y, et al. A dual-sphere coupled fiber optic photoacoustic (DSC-FOPA) sensor for CH_4 and C_2H_2 gases simultaneous detection in underground coal mines. Infrared Phys Technol, 2025: 105894
2 Su M, Chen S, Jiang B, et al. Determination the suppression effect and mechanism of C_2HF_5 on premixed ethylene-air explosion through experiment and simulation. Process Saf Environ Protection, 2025, 195: 106031
3 Bai J, Liang Y, Song S, et al. Explosion evolution characteristic of methane-acetylene mixtures under constant volume space. Combust Theor Model, 2025, 29: 125–144
4 Zha S, Chen H, Liu C, et al. Multivariate-coupled-enhanced photoacoustic spectroscopy with Chebyshev rational fractional-order filtering algorithm for trace CH_4 detection. Photoacoustics, 2025, 42: 100692
5 Rong Z, Ke J, Lu H, et al. A direct measurement of the C_2H_2 concentration from the C_2H_2-oil mixed solution using the photoacoustic spectroscopy method. Photonics, 2025, 12: 471
6 Lu D, Huang L, Zhang J, et al. Density functional theory investigation of pristine and ni-doped CeO_2 (110) for C_2H_4 detection based on optimized work functions. ACS Appl Nano Mater, 2024, 7: 4239–4251
7 Fu L, Zhang J, Pan Y, et al. Differential photoacoustic spectroscopy for flow gas detection based on single microphone. Photoacoustics, 2024, 38: 100624
8 Rong S, Sun X, Yang Y, et al. A trace C_2H_2 detection based on near-infrared dual-comb spectroscopy. Microw Opt Tech Lett, 2025, 67: e70073
9 Xu X H, Bi J, Zhang H, et al. Insight into low-temperature CH_2 combustion over CeO_2-Pd-$MgAl_2O_4$ catalysts by modulating metal-support interactions. Separation Purification Tech, 2025, 360: 131027
10 Wang Y, Xiang Q, Zhou Q, et al. First-principles prediction of Ni-MoO_3 as selective and sensitive sensor for detecting CO over CH_4, H_2, H_2O, NH_3, H_2S gases. Phys Lett A, 2024, 526: 129981
11 Allangawi A, Ayub K, Al-Saadi A A, et al. CO_2 reduction to CH_4: Harnessing $Fe_1@B_{12}N_{12}$ as single atom catalyst for environment restoration. Surfs Interfaces, 2025, 61: 106062
12 Chand Pal S, Krishna R, Das M C. Highly scalable acid-base resistant Cu-Prussian blue metal-organic framework for C_2H_2/C_2H_4, biogas, and flue gas separations. Chem Eng J, 2023, 460: 141795
13 Liu X, Zhang Z, Zhou J, et al. Artificial intelligence-enhanced waveguide "photonic nose"-augmented sensing platform for voc gases in mid-infrared. Small, 2024, 20: 2400035
14 Wang X Y. Photon-wave traveling model for analyzing spectral characteristics of light sources without resonant cavities. Sci China Inf Sci, 2025, 68: 199402
15 Tang Y, Zhao Y, Liu H. Room-temperature semiconductor gas sensors: challenges and opportunities. ACS Sens, 2022, 7: 3582–3597
16 Li Z, Zhang Q, Wang Z, et al. A highly sensitive low-pressure TDLAS sensor for detecting dissolved CO and CO_2 in transformer insulating oil. Optics Laser Tech, 2024, 174: 110622
17 Wang Y, Chen S, Kong Q, et al. Research on CO concentration detection based on deep learning and TDLAS technology. Optics Lasers Eng, 2024, 181: 108420
18 Huang A, Xu Z, Deng H, et al. High-pressure gas temperature sensing for exit plane of aero-engine combustor using tunable diode laser absorption spectroscopy. Microw Opt Tech Lett, 2024, 66: e33897
19 He Q, Feng Q, Li J. Long-term stable online acetylene detection by a CEAS system with suppression of cavity length drift. Sensors, 2019, 19: 508
20 Henderson B, Khodabakhsh A, Metsälä M, et al. Laser spectroscopy for breath analysis: towards clinical implementation. Appl Phys B, 2018, 124: 1–2
21 Zhao X, Wang H, Qi H, et al. Fiber optic photoacoustic gas sensor enhanced by multi-pass cell with overlapping phantom spots. Sens Actuat B-Chem, 2024, 412: 135816
22 Li J, Deng H, Sun J, et al. Simultaneous atmospheric CO, N_2O and H_2O detection using a single quantum cascade laser sensor based on dual-spectroscopy techniques. Sens Actuat B-Chem, 2016, 231: 723–732
23 Liu N, Xu L, Zhou S, et al. Simultaneous detection of multiple atmospheric components using an NIR and MIR laser hybrid gas sensing system. ACS Sens, 2020, 5: 3607–3616
24 Xu L, Zhou S, Liu N, et al. Multigas sensing technique based on quartz crystal tuning fork-enhanced laser spectroscopy. Anal Chem, 2020, 92: 14153–14163
25 Huang Q, Wei Y, Li J. Simultaneous detection of multiple gases using multi-resonance photoacoustic spectroscopy. Sens Actuat B-Chem, 2022, 369: 132234
26 Chen S L, Tian C. Recent developments in photoacoustic imaging and sensing for nondestructive testing and evaluation. Vis Comput Ind Biomed Art, 2021, 4: 6
27 Zhang C, Qiao S, He Y, et al. Trace gas sensor based on a multi-pass-retro-reflection-enhanced differential Helmholtz photoacoustic cell and a power amplified diode laser. Opt Express, 2023, 32: 848–856
28 Misztal K, Kopaczek J, Kudrawiec R. Photoacoustic spectroscopy of layered crystals: An enhancement of the photoacoustic signal and its analysis from the perspective of heat generation. Photoacoustics, 2025, 41: 100668
29 Xu S, Wang Q, Zhu Z, et al. Photoacoustic spectroscopy based on vertical cruciform multi-stepped photoacoustic cell achieving ppb-level acetylene detection. Sens Actuat B-Chem, 2024, 418: 136313
30 Zhao X, Wang H, Qi H, et al. Embedded T-type multi-pass cell based fiber-optic photoacoustic gas sensor. Sens Actuat B-Chem, 2024, 423: 136771
31 Wang G, Fu D, Yuan S, et al. Rapid detection of dissolved acetylene in oil based on T-type photoacoustic cell. Microw Opt Tech Lett, 2024, 66: e33793
32 Mao X, Ye H, Tan Y, et al. High sensitivity miniaturized multi-pass absorption enhanced differential Helmholtz photoacoustic gas sensor. Infrared Phys Tech, 2024, 137: 105142
33 Wu G, Ye H, Gong Z, et al. A new 3-D-printed nondestructive H-like resonant fiber-optic photoacoustic sensor for high-sensitivity remote gas sensing. IEEE Sens J, 2024, 24: 36946–36952
34 Feng Z, Sima C, Li T, et al. Ppb-level miniaturized flow gas sensor based on photoacoustic spectroscopy with advanced 3-D printed T-type resonant cell. IEEE Sens J, 2024, 24: 33962–33969
35 Ma Q, Li L, Gao Z, et al. Near-infrared sensitive differential Helmholtz-based hydrogen sulfide photoacoustic sensors. Opt Express, 2023, 31: 14851–14861

36 Wang F, Fu L, Wu J, et al. A compact photoacoustic detector for trace acetylene based on 3-D-printed differential Helmholtz resonators. IEEE Sens J, 2023, 23: 27207–27214
37 Zhang L, Liu L, Zhang X, et al. T-type cell mediated photoacoustic spectroscopy for simultaneous detection of multi-component gases based on triple resonance modality. Photoacoustics, 2023, 31: 100492
38 Gao Z, Li L, Liu M, et al. Photoacoustic trace gas detection of OCS using a 2.45 mL Helmholtz resonator and a 4823.3 nm ICL light source. Photoacoustics, 2024, 38: 100612
39 Li Z, Liu J, Si G, et al. Design of a high-sensitivity differential Helmholtz photoacoustic cell and its application in methane detection. Opt Express, 2022, 30: 28984–28996
40 Ma Y, Qiao S, He Y, et al. Highly sensitive acetylene detection based on multi-pass retro-reflection-cavity-enhanced photoacoustic spectroscopy and a fiber amplified diode laser. Opt Express, 2019, 27: 14163–14172
41 Zhang Q, Chang J, Cong Z, et al. Scanned-wavelength intra-cavity QEPAS sensor with injection seeding technique for C_2H_2 detection. Optics Laser Tech, 2019, 120: 105751
42 Dou D, Jiao M, Feng M, et al. Ppb-level photoacoustic detection of chloroform using four-microphone array. Anal Chem, 2025, 97: 1809–1815
43 Fu L, Wang F, Zhang J, et al. Miniaturization study on helmholtz-based photoacoustic cell for PAS-based trace gas detection. Measurement, 2024, 236: 115154
44 Xiang S, Gao S, Shi Y, et al. Experimental demonstration of a photonic spiking neuron based on a DFB laser subject to side-mode optical pulse injection. Sci China Inf Sci, 2024, 67: 132402
45 Lin S, Wang Z, Zhang J, et al. Radiation build-up and dissipation in Raman random fiber laser. Sci China Inf Sci, 2024, 67: 112402
46 Zhang M, Wu G, Gong Z, et al. A high-sensitivity compact dual-T-type resonant fiber-optic photoacoustic sensor for simultaneous detection of multiple gases. Sens Actuat B-Chem, 2024, 418: 136328
47 Burgués J, Jiménez-Soto J M, Marco S. Estimation of the limit of detection in semiconductor gas sensors through linearized calibration models. Anal Chim Acta, 2018, 1013: 13–25
48 Zhang C, Qiao S, He Y, et al. Multi-resonator T-type photoacoustic cell based photoacoustic spectroscopy gas sensor for simultaneous measurement C_2H_2, CH_4 and CO_2. Sens Actuat B-Chem, 2025, 427: 137168
49 Wang F, Fu L, Zhang J, et al. mL-level low gas consumption PAS sensor for dual gases CH_4/C_2H_2 detection based on an optimized TT-type resonator. Measurement, 2025, 242: 116288
50 Risser C, Parvitte B, Vallon R, et al. Optimization and complete characterization of a photoacoustic gas detector. Appl Phys B, 2015, 118: 319–326
51 Li C, Han X, Guo M, et al. Fiber-optic photoacoustic gas microsensor dual enhanced by Helmholtz resonator and interferometric cantilever. Anal Chem, 2024, 96: 9438–9446